

# Magneto-Optical and Multiferroic Properties of Transition-Metal (Fe, Co, or Ni)-Doped ZnO Layers Deposited by ALD

Albena Paskaleva,\* Krastyo Buchkov, Armando Galluzzi, Dencho Spassov, Blagoy Blagoev, Tzvetan Ivanov, Vladimir Mehandzhiev, Ivalina Avramova Avramova, Penka Terzyiska, Peter Tzvetkov, Daniela Kovacheva, and Massimiliano Polichetti



Cite This: *ACS Omega* 2022, 7, 43306–43315



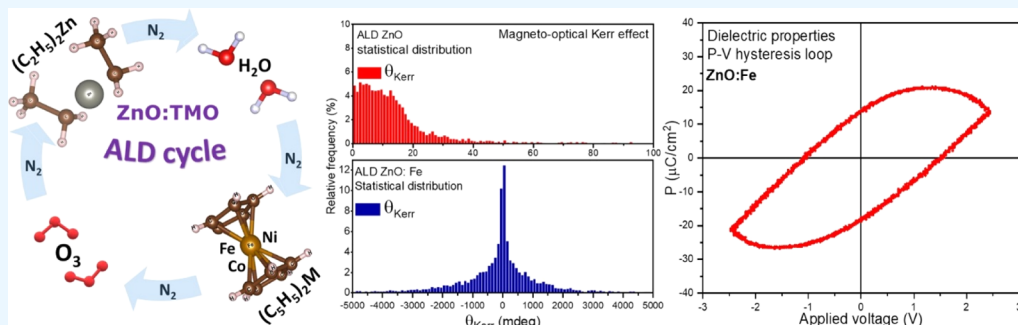
Read Online

ACCESS |

Metrics & More

Article Recommendations

Supporting Information



**ABSTRACT:** ZnO doped with transition metals (Co, Fe, or Ni) that have non-compensated electron spins attracts particular interest as it can induce various magnetic phenomena and behaviors. The advanced atomic layer deposition (ALD) technique makes it possible to obtain very thin layers of doped ZnO with controllable thicknesses and compositions that are compatible with the main microelectronic technologies, which further boosts the interest. The present study provides an extended analysis of the magneto-optical MO Kerr effect and the dielectric properties of (Co, Fe, or Ni)-doped ZnO films prepared by ALD. The structural, magneto-optical, and dielectric properties were considered in relation to the technological details of the ALD process and the corresponding dopant effects. All doped samples show a strong MO Kerr behavior with a substantial magnetization response and very high values of the Kerr polarization angle, especially in the case of ZnO/Fe. In addition, the results give evidence that Fe-doped ZnO also demonstrates a ferroelectric behavior. In this context, the observed rich and versatile physical nature and functionality open up new prospects for the application of these nanostructured materials in advanced electronic, spintronic, and optical devices.

## 1. INTRODUCTION

ZnO and ZnO-based materials are one of the most extensively studied materials because of the numerous advantages and possible applications in a broad range of opto-, micro-, nano-, and acoustoelectronic devices.<sup>1–4</sup> ZnO is a wide band-gap n-type semiconductor with a large excitonic binding energy. It is chemically stable; it has a good electrochemical activity and is biocompatible and environmentally friendly. ZnO films can be easily and successfully prepared by almost all deposition techniques—magnetron sputtering, pulsed laser deposition, sol–gel spin coating, spray pyrolysis, chemical vapor deposition, atomic layer deposition (ALD), and so forth, resulting in a broad range of 1D, 2D, and 3D morphologies/microstructures. Consequently, mechanical, chemical, electrical, and optical properties of ZnO could be modified and improved by the growth process and related process parameters, including annealing steps. Another efficient way to tailor and enhance the ZnO properties is by doping with different elements. The dopant and its concentration in the

ZnO matrix should be carefully chosen and optimized in order to achieve the desired behavior. All this makes ZnO a very versatile material whose properties can be properly tuned according to the specific requirements of the application. Moreover, it is possible to increase the functionality of ZnO by simultaneous control over more than one parameter, which opens up a wide range of exciting applications.

From this point of view, doping with transition metals (TMs) Co, Ni, Mn, or Fe is of particular interest as they have partially filled d-states, and hence, they contain non-compensated spin of electrons, which can induce magnetic behavior/phenomena (ferromagnetism and magnetoresist-

Received: September 27, 2022

Accepted: November 3, 2022

Published: November 14, 2022



ance). Diluted magnetic semiconductors (DMSs) (i.e., semiconductors with net spin polarization—e.g., ZnO in which magnetic TM ions substitute cations of the host semiconductor material) are especially attractive for spintronics and micro(nano)electronics as they allow realization of simultaneous control over the electronic state and carrier dynamics in the semiconductor and the robustness and coherence of the magnetic spin of the TM. Room-temperature (RT) ferromagnetism (FM) in Mn-doped p-type ZnO has been predicted by Dietl et al.<sup>5</sup> First-principles calculations<sup>6,7</sup> based on density functional theory (DFT) also predicted FM in the most of the 3d TM-doped ZnO materials. Soon after, RT FM in doped ZnO was also experimentally observed, which consequently triggered intensive investigations.<sup>8–10</sup> Several mechanisms explaining the RT FM in TM-doped ZnO films have been proposed.<sup>11</sup> The most widely accepted are as follows: (i) the Ruderman–Kittel–Kasuya–Yoshida (RKKY), which results from the coupling mechanism related to the *d* shell electron spins mediated by conduction electrons interactions and (ii) the mechanism of bound magnetic polarons (BMPs) formed by the s–d exchange interactions between the electron spin of the nanoscale defect (e.g., vacancy, secondary phase, etc.) and the electron spins of substitutional 3d TM ions.<sup>12,13</sup>

The magneto-optical (MO) properties of ZnO-based DMSs are also of particular interest as they allow us to combine the good optical transparency of ZnO together with magnetism. MO phenomena [magnetic circular dichroism,<sup>14,15</sup> the MO Faraday effect,<sup>16</sup> and the MO Kerr effect<sup>17,18</sup> (MOKE)] are interesting both from the fundamental point of view and for the application in various devices such as information storage systems, magnetic field sensors, optical isolators, and so forth. In the MOKE technique, the change in the linear polarization of the light reflected from the magnetic surface in a direct relation to the microscale magnetic hysteresis is studied. The MOKE is a powerful tool to study the local electronic and magnetic properties of materials.<sup>19–21</sup> Enhancement of the MOKE can be obtained by a careful design of materials (including their thickness) and structures, for example, a large Kerr rotation angle reaching several degrees was reported for structures consisting of stacked magnetic and dielectric thin films; Fabry–Perot cavities; 1D photonic crystals; and so forth.<sup>22–24</sup>

ZnO has a hexagonal wurtzite structure (non-centrosymmetric  $P6_3mc$  space group) and possesses intrinsic polarization along the *c*-axis due to cation and anion tetrahedral alignment in that direction. However, a large coercive field (>7 MV/cm) is needed for switching;<sup>25</sup> hence, ferroelectricity in pure defect-free ZnO is difficult to observe. Incorporating optimized dopants in ZnO can induce switchable polarization more effectively and easily. Ferroelectricity in doped ZnO is usually explained with the difference in the ionic radii of dopant and  $Zn^{2+}$  ions. Because of this difference, the dopant occupies an off-centered position, which results in the formation of a permanent electrical dipole.<sup>26–28</sup> Therefore, ferroelectricity in doped ZnO is most often reported for dopants with a relatively smaller/larger ionic radius [e.g.,  $V^{2+}$  (0.93 Å) and  $Cr^{3+}$  (0.63 Å)] with respect to  $Zn^{2+}$  (0.74 Å). The coexistence of FM and ferroelectricity in doped ZnO has also been reported in several studies.<sup>29–31</sup>

Among the deposition methods, ALD of ZnO layers as well as its doped counterparts has attracted increased attention recently as it enables the deposition of very thin (several

nanometers) homogeneous films with superior quality, which could be implemented in a wide variety of devices.<sup>32</sup> Moreover, ALD is CMOS-compatible, which allows integration of ZnO layers in micro- (nano-)electronic devices, including semiconductor spintronic devices. However, there are only a few reports that study TM (Ni, Co, and Fe)-doped ZnO films prepared by ALD, and these are confined to Co-doped ZnO films.<sup>32</sup>

In this work, MO and dielectric properties of Ni-, Co-, or Fe-doped ZnO layers deposited by ALD have been investigated. To the best of our knowledge, this is the first study that reports the MO and dielectric behavior of ZnO layers deposited by ALD and doped with various TMs (Fe, Ni, and Co) and compares their properties in dependence on the dopant.

## 2. EXPERIMENTAL PROCEDURE

**2.1. Deposition of Films.** A standard thermal ALD process using a Beneq TFS-200 reactor system has been used to deposit TM (Ni, Fe, or Co)-doped ZnO films. To obtain a ZnO matrix, diethylzinc (DEZ) as a Zn precursor and deionized (DI) water as an oxidant have been used, whereas for TM doping, a metallocene ( $MCp_2 = NiCp_2$ ;  $CoCp_2$ ; and  $FeCp_2$ ) precursor and ozone  $O_3$  have been used. The ALD system is equipped with HS-300 hot source containers to supply the solid metallocene precursors. The ZnO/TM supercycle consists of 16 cycles of DEZ/DI  $H_2O$  followed by five cycles of  $MCp_2/O_3$ , and it is repeated 24 times. The deposition is performed at 180 °C. Each precursor and oxidant pulse has been followed by a pure nitrogen purging at 300 sccm flow. The pulse duration and purging times (*p*) for both subcycles have been as follows: DEZ/*p*/DI  $H_2O$ /*p* = 0.2/2/0.2/2 s and  $MCp_2$ /*p*/ $O_3$ /*p* = 2/4/1/5 s, respectively. The metallocene precursor has been heated up to 80 °C in order to enhance the sublimation process, hence its vapor pressure. The ALD process sequence is presented schematically in Figure S1. The films were deposited on p-type (100) Si substrates covered with a native  $SiO_2$  layer. The thickness of the deposited TM-doped ZnO layers has been measured ellipsometrically and is about 75 nm.

Metal-doped ZnO–metal (MOM) structures with a bottom electrode of TiN and a top electrode of Pt have been prepared for electrical measurements. The top Pt electrodes (circles with an area of  $A = 1.96 \times 10^{-3} \text{ cm}^2$ ) were deposited through a shadow mask.

**2.2. Material Characterization.** The X-ray diffraction (XRD) patterns were collected within the  $2\theta$  range from 10 to 80° with a constant step of 0.02° on a Bruker D8 ADVANCE diffractometer with Cu  $K\alpha$  radiation and a LynxEye detector at RT. The phase identification was performed using the DifracPlus EVA program using the ICDD-PDF2 Database. The unit cell volume and parameters were determined by the whole powder pattern fitting procedure (Pawley fit) using the Bruker TOPAS v.4.2 program.<sup>33,34</sup> The crystallographic structure visualization was performed using VESTA software.<sup>35</sup>

The MO Kerr parameters were acquired using a magneto optical Kerr magnetometer NanoMOKE<sup>3</sup> under a longitudinal field experimental setup based on a scanning laser microscope probe operating at  $\lambda = 660$  nm, with an integrated optical system with a pair of galvanometric mirrors. The maximal magnetic field range is 4000 Oe with a varying frequency of 2.1 Hz. The MOKE experiment is based on the measurement of the polarization change of the reflected light defined by the

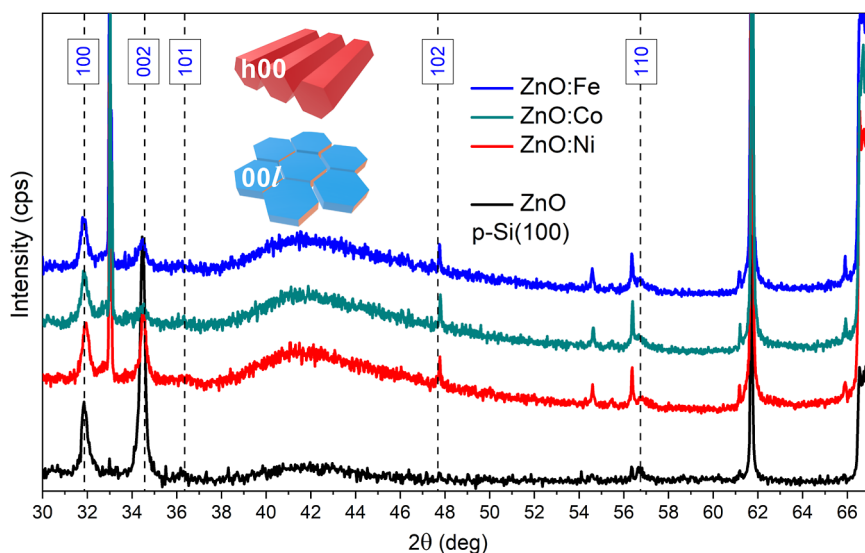


**Figure 1.** XRD pattern comparisons of undoped ZnO and Fe, Co, and Ni doped ZnO layers with corresponding crystallographic ( $hkl$ ) peak designations.

magnetization nature of the material surface in relation with the spin and domain wall dynamics. The MO response is described theoretically<sup>36</sup> by the elements of the general dielectric tensor (within the frame of the Jones matrix formalism) since the measured (at selected points and regions) hysteresis dependencies of the Kerr rotation versus field are also proportional to the localized magnetization, which allows indirect estimation of the coercivity  $H_c$ . The mapping of the material's Kerr magnetization properties—the Kerr angle ( $\theta_{\text{Kerr}}$ ) and the related coercivity  $H_c$ —has been obtained over different sectors with magnetic pixel resolutions of  $\sim 5$  and  $10 \mu\text{m}$ .

Dielectric properties of doped ZnO films have been assessed by measuring capacitance–frequency ( $C-f$ ) and capacitance–voltage ( $C-V$ ) curves via an LCR meter (Agilent E4980A) at RT in a frequency range of  $10^3$  to  $10^6$  Hz. The ferroelectric properties were evaluated on the Sawyer–Tower circuit using a Keysight DSOX1204G digital oscilloscope. Triangular AC voltage was used with an amplitude of 2.5 V and  $f = 1.5$  and 3 kHz provided by the DSOX1204G built-in signal generator.

### 3. RESULTS AND DISCUSSION

**3.1. X-Ray Diffraction Analysis.** The diffraction patterns of pure and TM-doped ZnO are presented in Figure 1. A textured polycrystalline layer of nanosized ZnO with a predominant intensity of (100) and (002) index reflections, which confirms the formation of ZnO with a hexagonal wurtzite structure, is observed for all films. While the intensity of reflections with index (100) remains almost the same for all samples, the intensity of (002) reflections varies depending on the doping element. A similar dependence between the intensities of (100) and (002) reflections is also observed for thin films with a low degree of TM doping (with less TM deposition cycles).<sup>37,38</sup> Our previous studies revealed that the intensities of the measured ZnO reflections changed significantly depending also on both the deposition temperature<sup>39</sup> and the degree of Al doping.<sup>40</sup> The present results demonstrate that in pure ZnO thin films, the orientation along the  $c$ -axis direction is significantly better expressed, which is proved by the high intensity of reflections with index (002). In

contrast, only reflections with index (100) were observed in the Co-doped samples, indicating a change in the orientation of the ZnO crystallites with an  $ab$ -plane perpendicular to the substrate. In Ni- and Fe-doped thin films both orientations (100) and (002) ( $ab$ - and  $c$ - oriented respectively) are present. For Fe-doped sample, the intensity of the (100) peak is substantially larger, that is, it is the preferred orientation. It is also seen that in addition to (100) and (002), a low intensity diagonal reflex (102), which is not observed in pure ZnO, also appears (Figure 1). Therefore, it could be concluded that in TM-doped ZnO films, disorientation increases. It should be mentioned that no diffraction peaks different from those related to ZnO and the Si substrate have been observed. The amorphous halo at about  $2\theta = 41.5^\circ$  is observed in all samples (including the bare Si substrate before ZnO deposition) and is due to the thin SiO<sub>2</sub> layer on the surface. During the deposition of ZnO, the Si substrate is additionally oxidized, and this oxidation is stronger in the case of doped ZnO layers as the ozone used in TM deposition cycles is a stronger oxidizing agent than the DI water used in ZnO deposition cycles. As a result, the intensity of the amorphous halo at  $2\theta = 41.5^\circ$  increases for doped ZnO.

The ZnO unit cell parameters and crystallite size (CS) for all samples (Table 1) were calculated using the Pawley fit whole profile fitting procedure as implemented in Bruker Topas v.4.2 software.<sup>33,34</sup> The instrumental broadening correction was calculated using the fundamental parameters approach.<sup>41</sup> The unit cell parameters of investigated TM-doped ZnO thin films are equal (within the systematic error) to the reference values

**Table 1.** Cell Parameters and CS of Undoped ZnO and TM-Doped ZnO

sample	ZnO on p-Si (100)		
	$a$ (Å)	$c$ (Å)	CS (nm)
ZnO (oxygen deficient)	3.242(2)	5.204(3)	38(2)
ZnO	3.244(1)	5.208(1)	34.6(8)
ZnO/Ni	3.238(1)	5.202(2)	28.4(12)
ZnO/Co	3.240(1)	5.204(3)	20.5(12)
ZnO/Fe	3.240(1)	5.202(2)	23.2(12)

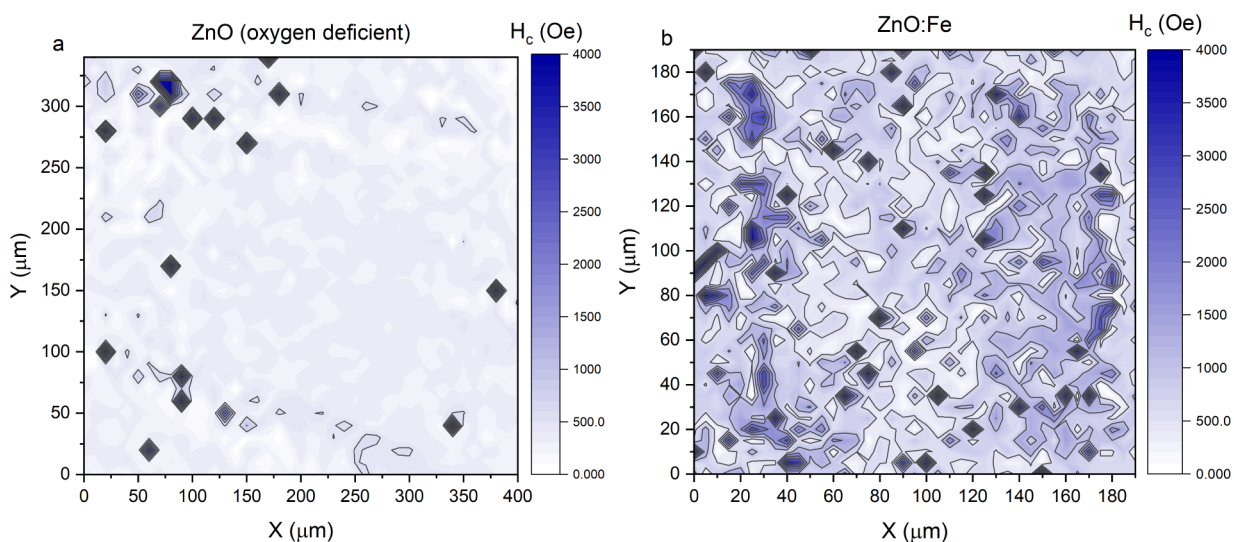


**Figure 2.** Maps of the coercivity variations for (a) ZnO (oxygen deficient) and (b) ZnO/Fe ALD layers.

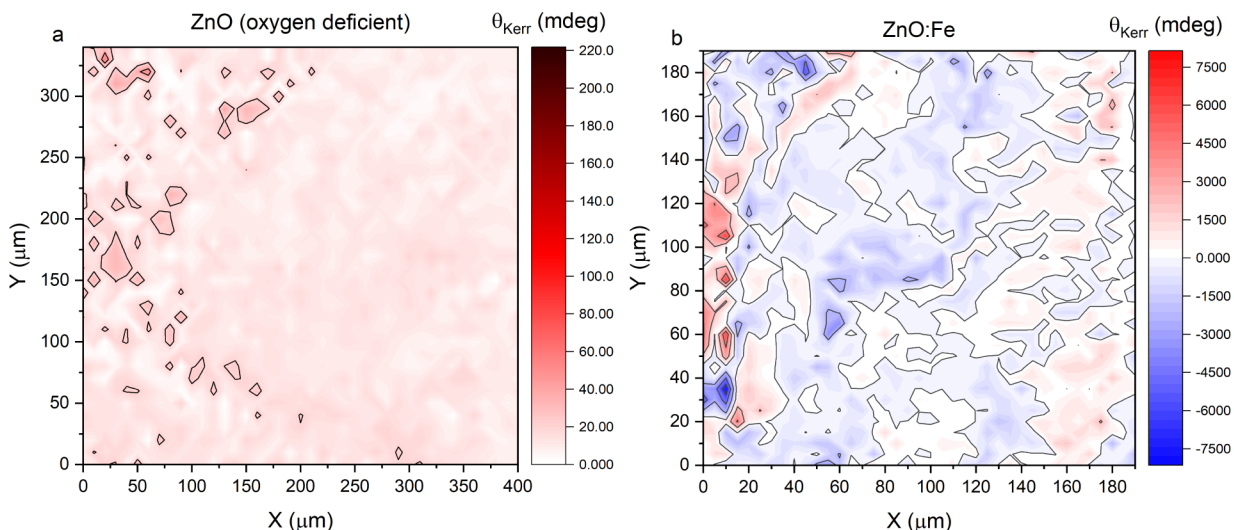


**Figure 3.** Maps of the Kerr angle variations for (a) ZnO (oxygen deficient) and (b) ZnO/Fe ALD layers.

for ZnO (ICDD PDF-2 card no. 00-036-1451, SG:186,  $a = 3.242 \text{ \AA}$ ;  $c = 5.207 \text{ \AA}$ ). Having in mind that the difference of the ionic radii of  $Zn^{2+}$ ,  $Co^{2+}$ ,  $Fe^{2+}$ , and  $Ni^{2+}$  is less than 10%, together with the relatively low level of doping, it is expected that the doping should not affect the crystal metrics of the ZnO matrix. A small difference is observed for the  $a$ -parameter of Ni-doped ZnO, most likely due to defects in the oxygen sublattice. The mean CSs of pure and doped ZnO films were also calculated (Table 1). The mean CS of pure ZnO is obtained in the range 35–38 nm, while those of all doped counterparts are in the range 20–30 nm, that is, the doping results in a reduction of the CS. In comparison to the more lightly TM-doped ZnO (with the CS in the range 35–60 nm),<sup>38</sup> the present more heavily doped ZnO samples have a smaller CS. Among the various doped layers, Ni-doped ZnO has the largest CS—a result observed in both lightly and heavily doped films.

**3.2. Magnetic Coercivity and MO Kerr Rotation Angle of the Polarization.** The magnetic properties of Co-, Fe-, and Ni-doped ZnO and reference ZnO ALD layers were investigated within the frames of the MOKE. To evaluate

the possible impact of oxygen vacancies,  $V_o$ , on the magnetic response of ZnO layers, two ZnO layers with different amounts of  $V_o$  (as assessed by X-ray photoelectron spectroscopy, Supporting Information Figure S2) have been investigated. Color gradient maps of the coercivity  $H_c$  and of the Kerr polarization rotation angle  $\theta_{Kerr}$  at the magnetization saturation have been constructed by measuring multiple Kerr hysteresis loops for each selected point. The behavior of the primary MOKE characteristics was analyzed over several sectors on the film surface. For the purpose of clarity, selected  $H_c$  and  $\theta_{Kerr}$  gradient maps only of undoped (oxygen deficient) ZnO and Fe-doped ZnO layers are shown in Figures 2 and 3. The  $H_c$  and  $\theta_{Kerr}$  maps of Ni- and Co-doped ZnO are similar to those of the ZnO/Fe layer. The corresponding coercivity map of the undoped ZnO (oxygen deficient) is uniform (Figure 2a); the observed locations with very high  $H_c$  are stochastically distributed and can be assigned to the measurement artefacts. The  $H_c$  magnitude, the level of inhomogeneity and the overall magnetization is significantly stronger for the Fe-doped sample (Figure 2b). For undoped ZnO, only clockwise Kerr rotation (i.e., positive  $+\theta_{Kerr}$  values) is observed (Figure 3a). Generally,

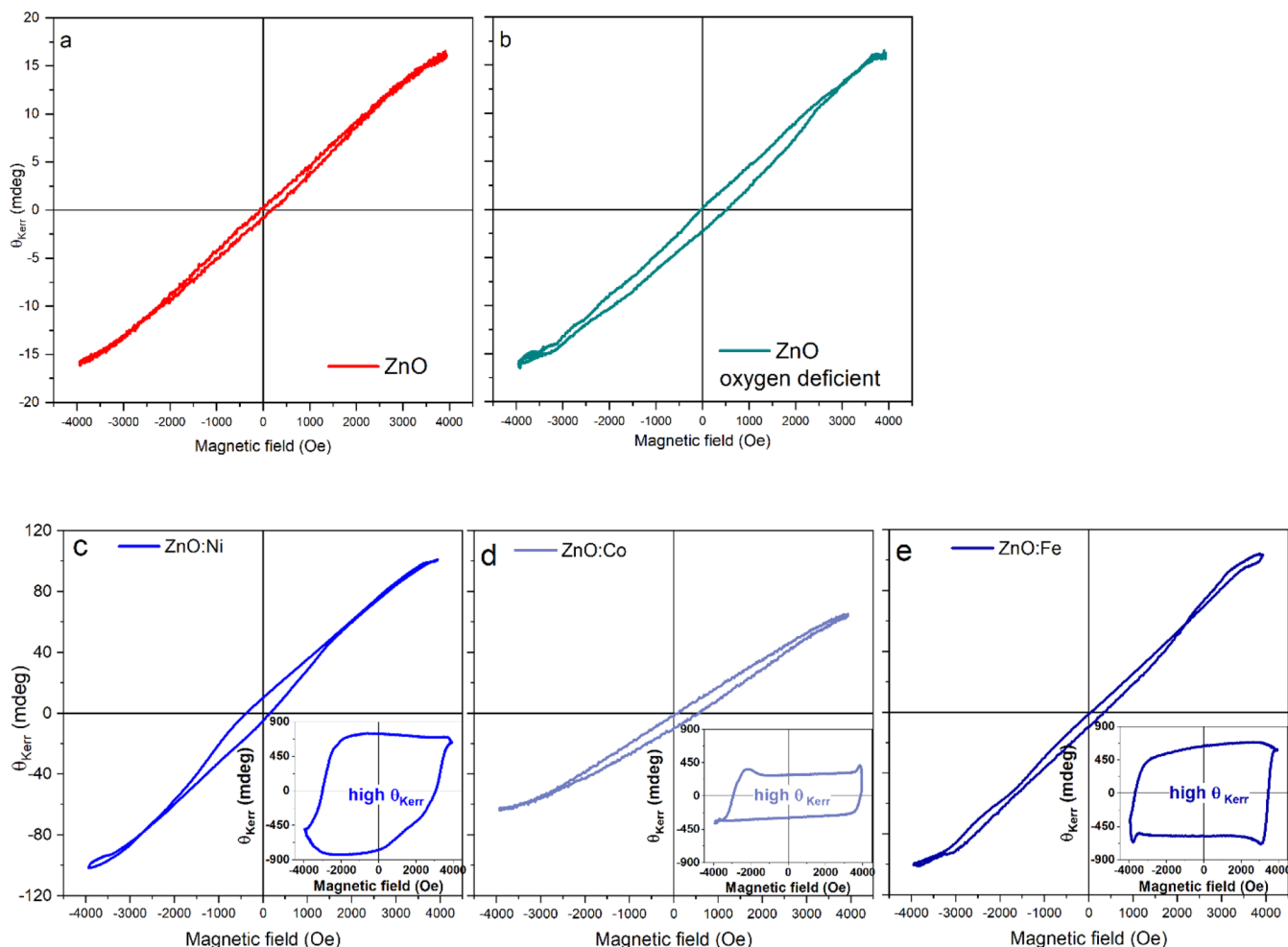


**Figure 4.** Selected  $\theta_{\text{Kerr}}$  vs field hysteresis loops for (a) ZnO; (b) oxygen-deficient ZnO; and (c) Ni-, (d) Co-, and (e) Fe-doped ZnO layers. The insets show example curves with large hysteresis and Kerr angle values.

both undoped ZnO layers are homogeneous, and the values of  $\theta_{\text{Kerr}}$  are very small—most of the data are in the range [0–20] mdeg. There are isolated locations where  $\theta_{\text{Kerr}}$  reaches values as high as 100 mdeg. Similarly to  $H_c$  maps, the Kerr angle map of Fe-doped ZnO (Figure 3b) differs substantially from that of the undoped film. The ZnO/Fe layer demonstrates inhomogeneous distribution of  $\theta_{\text{Kerr}}$  whose values are significantly (2 orders of magnitude) larger than those of the undoped layer. Another interesting feature is that both clockwise (positive  $\theta_{\text{Kerr}}$ ) and counterclockwise (negative  $\theta_{\text{Kerr}}$ ) Kerr polarization rotations are observed, indicative of complex MO process activity.

The inhomogeneity is also demonstrated in Figure 4a–e where example  $\theta_{\text{Kerr}}-H$  curves for undoped and TM-doped ZnO layers are presented. The observed complex micro MOKE (diffracted and asymmetrical) hysteresis loops, particularly for the TM-doped samples, reveal the variations and non-uniformity of the MO response. As is seen, these variations are significant in the case of TM-doped layers and for a certain fraction of the measurements with broad hysteresis contours, and  $\theta_{\text{Kerr}}$  can reach significant values at the maximum applied field. To account for these large variations and to get more information on their origin, the statistical distributions of the coercivity and Kerr angle are considered below.

The descriptive statistical dispersion and variability of the acquired data are systematized in an comparative overview for all investigated layers and presented in Figures 5 and 6. For the sake of simplicity, the statistical distributions are divided in three intervals of small  $H_c < 500$  Oe, medium  $500 \text{ Oe} < H_c < 1000$  Oe, and large  $H_c > 1000$  Oe coercivities and are presented in the form of a pie chart diagram in the right hand side of the figure. Similarly, for the Kerr rotation angle, the regions are defined as follows: small  $|\theta_{\text{Kerr}}| < 100$  mdeg, medium  $100 \text{ mdeg} < |\theta_{\text{Kerr}}| < 1000$  mdeg, and large  $|\theta_{\text{Kerr}}| > 1000$  mdeg.

The undoped ZnO films show a weak magnetic behavior with the highest frequency (78%) of small coercivity values. The magnetic behavior of ZnO is very often assigned to the existence of oxygen vacancies  $V_o$ .<sup>12,42</sup> To account for this possibility, two ZnO layers with different amounts of  $V_o$  have been studied. As is seen from the statistic comparisons, the layer with the increased amount of  $V_o$  indeed reveals increased relative frequencies of the medium ( $500 \text{ Oe} < H_c < 1000$  Oe) range. However, the magnetic behavior of all doped counterparts differs substantially from that of pure ZnO (including the ZnO sample with increased  $V_o$ ), which excludes the vacancies as the main reason for the induced magnetic properties.

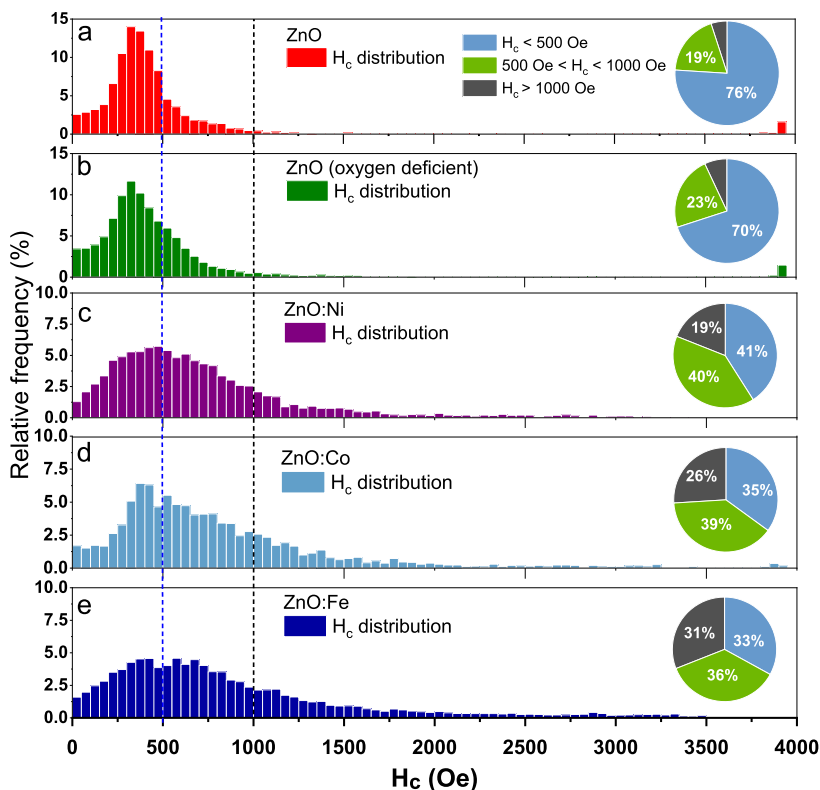


**Figure 5.** Statistical distributions of  $H_c$  variation for (a) ZnO; (b) oxygen-deficient ZnO; and (c) Ni-, (d) Co-, and (e) Fe-doped ZnO layers.

For all doped layers, the  $H_c$  statistical dispersions presented in Figure 5a–e are relatively broad; nevertheless, several tendencies are clearly observed:

- Magnetization for all TM-doped ZnO layers increases substantially—the regions with small magnetization decrease to about 33–41% (in dependence on the dopant) compared to more than 70% for the undoped layers. Respectively, the frequencies of medium and large magnetization values increase.

The major percentage fraction with  $H_c > 500$  Oe, that is, medium and large coercivity values, depends on the dopant and increases with the doping element in the following order—Ni, Co, and Fe. In the same order does the fraction of high magnetization values increase also:  $H_c > 1000$  Oe—ZnO/Ni—19%, ZnO/Co—26% and ZnO/Fe—31%. It should be noticed that this order follows precisely the order of the corresponding free (unpaired) 3d spins: Ni( $\uparrow$ )—one, Co( $\uparrow\uparrow$ )—two, and Fe( $\uparrow\uparrow\uparrow$ )—three unpaired spins.

It is known that the MOKE is proportional to spin–orbit interaction and net spin polarization; hence, it preferentially senses magnetic electrons (i.e., in our case 3d electrons).<sup>43</sup> Therefore, these results unambiguously demonstrate that the observed magnetic behavior of TM-doped ZnO layers stems from the magnetic properties of the dopant; hence, they give evidence that the applied ALD scheme resulted in the formation of a (diluted) magnetic semiconductor.<sup>14</sup> A possible formation of TM clusters and/or TM oxides could also add to the increased magnetic response of the layers. However, having in mind the similar behavior of all TM-doped layers and dissimilar magnetic properties of their respective TM oxides (e.g., NiO is antiferromagnetic and Fe oxides are ferromagnetic), we can exclude TM oxides as a dominant reason for the

observed strong MO response of the layers. In addition, XRD spectra do not show any peaks that may be related to TM phases.

The statistical distribution of  $\theta_{\text{Kerr}}$  values (Figure 6a–e) demonstrates in a more straight forward way the substantial qualitative and quantitative difference between the pure and TM-doped ZnO films. The undoped ZnO layers reveal very weak MO activity with the majority of  $\theta_{\text{Kerr}}$  values less than 20 mdeg (Figure 6a,b). All TM-doped layers (Figure 6c–e) exhibit very large  $\theta_{\text{Kerr}}$  values, which are symmetrically distributed with respect to 0. Depending on the dopant, similar trends to those observed for the coercivity appeared from the  $\theta_{\text{Kerr}}$  distributions. The fraction with  $|\theta_{\text{Kerr}}| > 100$  mdeg increases with the dopant in the order Ni, Co, and Fe. The fraction of very large  $|\theta_{\text{Kerr}}| > 1000$  mdeg increases in the same order, that is, 12% for ZnO/Ni; 20% for ZnO/Co, and 33% for ZnO/Fe. It should be noted that for ZnO/Fe,  $\theta_{\text{Kerr}}$  values as high as  $5^\circ$  have been observed, while for the other two dopants, the maximal  $\theta_{\text{Kerr}}$  reaches  $\sim 2^\circ$ . The fact that the identified giant MO Kerr rotation is characteristic for all TM-doped layers and symmetric around the zero suggests a common underlying MO mechanism. It is also seen that the strength of the Kerr effect is correlated with the magnetization, that is, the maximal Kerr rotation is observed for ZnO/Fe, which reveals the largest  $H_c$  and vice versa—the weakest MOKE is demonstrated by ZnO/Ni, which has the smallest observed magnetization. This is consistent with the expected trend for ferromagnetic materials that the Kerr angle increases with magnetization.<sup>34</sup> The broadly varied MO Kerr parameters are dependent on localized Fe, Co, and Ni concentration variations, implying randomized inhomogeneous distribution of the dopants in the crystal structure.<sup>17</sup> On the other hand, considering the alternating layer by layer (ZnO

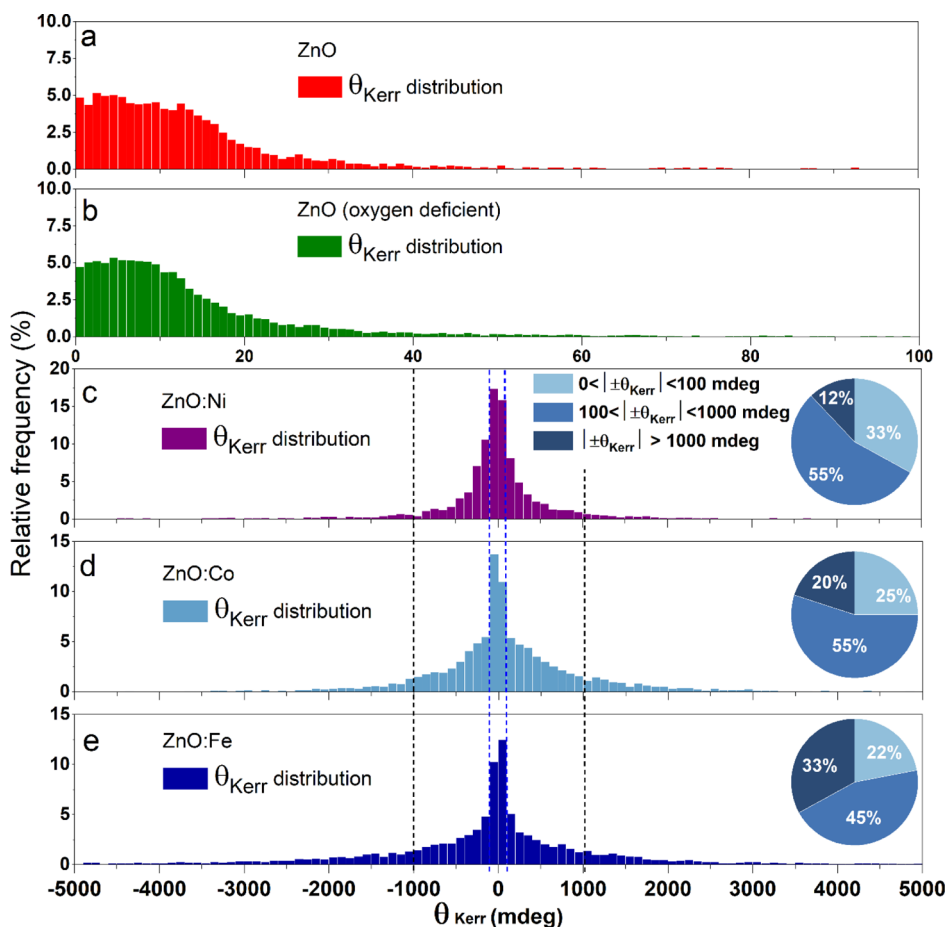


**Figure 6.** Statistical distributions of Kerr angle variations for (a) ZnO; (b) oxygen-deficient ZnO; and (c) Ni-, (d) Co-, and (e) Fe-doped ZnO layers.

and TMO) deposition process of the ALD technique, we have to point out the significant MOKEs detected in ZnO-based MO cavity/dielectric (with low optical losses) nano-laminates (Fabry–Perot type).<sup>23,24,44,45</sup> The optical enhancement (several orders of magnitude) of MO Kerr polarization rotation in such structures is related to internal interference effects and the addition of multiple reflections in the nanolayered architecture—dependent on the layer arrangement, thickness, and the reflective properties of the substrate material. We suppose that the observed extreme variations in the MO Kerr response are related to the complex synergistic influence of all noted factors. Various types of materials demonstrate such enhanced MOKE polarization rotation, some of which share the similar universal multiferroic nature to that for the investigated TMO/ZnO layers—nanostructured plasmonic dielectrics,<sup>46</sup> artificially nano-engineered metamaterials,<sup>47</sup> 2D TM dichalcogenides, and topological insulators.<sup>48</sup>

**3.3. Dielectric and Ferroelectric Properties.** Variations of the dielectric constant,  $\epsilon_r$ , and the dielectric loss ( $\tan \delta$ ) of the samples in the frequency range 1 kHz to 1 MHz are shown in Figure 7a,b. A strong frequency dependence of the dielectric constant is observed, especially for Fe- and Ni-doped ZnO. Various polarization mechanisms (ionic, orientation, and space charge) can exist in the layers and give rise to an increased polarization (hence  $\epsilon_r$ ) at a certain frequency. For ZnO/Fe,  $\epsilon_r$  changes only slightly in the range  $f = 10^3$ – $10^5$  Hz, and for  $f > 10^5$  Hz, a steep decrease is observed. For the ZnO/Ni film, it is seen that there is another polarization mechanism, which is

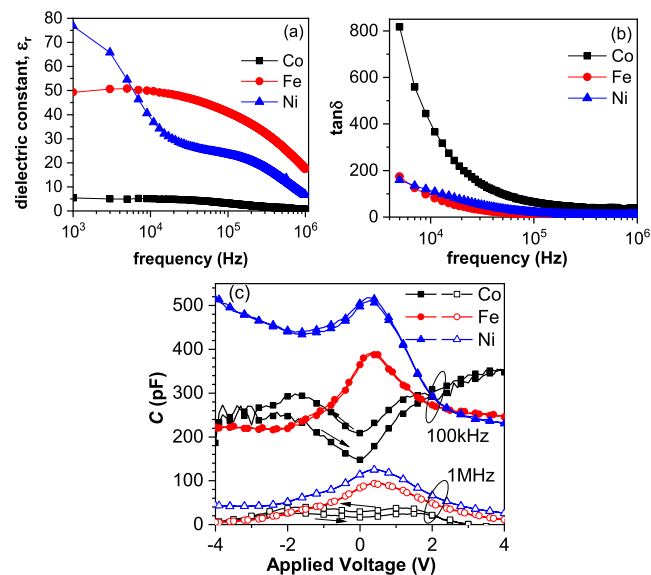


**Figure 7.** Frequency dependence of (a) dielectric constant  $\epsilon_r$  and (b) dielectric loss  $\tan \delta$  and (c) capacitance–voltage characteristics of TM-doped ZnO films.

involved at  $f = 10^3$ – $10^4$  Hz and significantly increases  $\epsilon_r$  in this frequency range. The most likely polarization mechanism, which adds to the net polarizability in the range  $10^3$ – $10^5$  Hz, is the orientation (dipolar) polarization.<sup>49</sup> We suggest that the

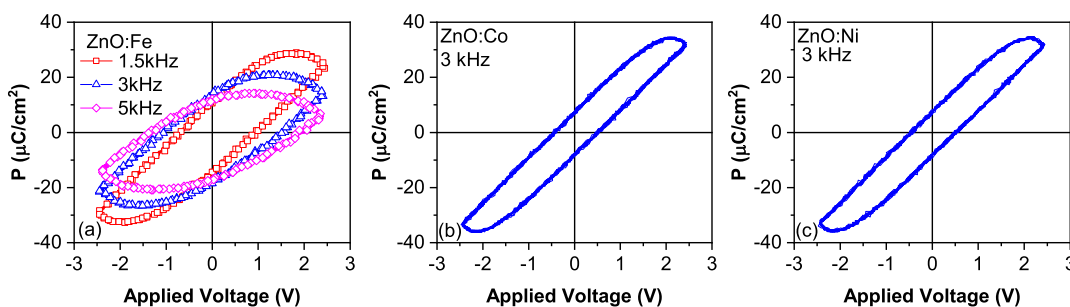


**Figure 8.**  $P$ – $V$  hysteresis loops for (a) Fe-; (b) Co-; and (c) Ni-doped ZnO films.

substitution of dopant ions at Zn sites results in Fe–O (Ni–O) bond formation. These bonds are non-collinear and rotate more easily, thus enhancing the dielectric response of the layer.<sup>50</sup> The present results suggest that dipolar polarization is stronger in Fe-doped ZnO. Another mechanism that can substantially increase polarization is the charge build-up and polarization at grain boundaries and/or heterointerfaces (also known as Maxwell–Wagner polarization). From this point of view, the formation of NiO clusters in the ZnO matrix, which was suggested to occur in similar layers with lower Ni doping,<sup>37</sup> is a possible explanation for the increased  $\epsilon_r$  at  $f = 10^3$ – $10^4$  Hz. It should be noted that the calculated static dielectric constant  $\epsilon_r$  of Fe- and Ni-doped ZnO layers is significantly larger than that of the host ZnO, which is usually reported to be  $\epsilon_r = 8$ – $9$ .<sup>51</sup> Recently, Végesna et al.<sup>51</sup> attributed the increase of the static dielectric constant in magnetic n-type Co- and Mn-doped ZnO layers to the contribution of BMPs to the electrical polarization. These polarons are formed by s–d exchange interaction between electron spins of the positively charged oxygen vacancy  $V_o^+$  in the BMP center and the electron spins of substitutional dopant ions. Having in mind the ferromagnetic behavior of the Fe- and Ni-doped ZnO, as observed in the previous section, it can be concluded that the increased static dielectric constant may be indeed partly due to BMPs. The dielectric response of the ZnO/Co film is significantly weaker than that of the other two films— $\epsilon_r$  is substantially smaller than that of ZnO/Ni and ZnO/Fe films; it is also smaller than that of pure ZnO layers. However, it should be noticed that the measurement of  $C$ – $f$  curves is performed at a small voltage (0.3–0.5 V) where the capacitance of the ZnO/Co film has the minimum in the  $C$ – $V$  curves, while that of the other two films reaches its maximum, as shown in Figure 7c.

In Figure 8, the ferroelectric  $P$ – $V$  hysteresis loops for TM-doped ZnO films measured on a Sawyer–Tower circuit are shown. The Fe-doped layers (Figure 8a) reveal a ferroelectric-like behavior with a well-resolved  $P$ – $V$  loop and the polarization increasing with the decreasing frequency. The results for Ni- and Co-doped layers, though showing some  $P$ – $V$  hysteresis, are not that convincing for the existence of ferroelectricity. It should be mentioned that all layers have a relatively high dielectric loss (Figure 7b), which is due to the increased conductivity of the layers. This could compromise the shape of the  $P$ – $V$  loop as well as the values of  $P$ , which are much higher than usually reported for ZnO-based materials. The observed stronger ferroelectric behavior of Fe-doped ZnO is in a very good agreement with the observed higher  $\epsilon_r$  of ZnO/Fe layers in the range  $f = 10^4$ – $10^6$  Hz as compared to the other films (Figure 7a) and the suggested domination of dipolar polarization in this frequency range for the ZnO/Fe film. It should be mentioned also that among the three TMs

used,  $\text{Fe}^{3+}$  has the smallest radius ( $\text{Fe}^{3+}$ —0.63 Å;  $\text{Ni}^{2+}$ —0.69 Å; and  $\text{Co}^{2+}$ —0.72 Å) with respect to  $\text{Zn}^{2+}$  (0.74 Å), which can explain its strongest ferroelectric response.

## 4. CONCLUSIONS

Thin TM (Fe, Co, or Ni)-doped ZnO films are successfully deposited by ALD. The study of their MO properties reveals that all TM-doped layers have qualitatively and quantitatively different behaviors compared to that of pure ZnO. All doped films demonstrate a very strong MOKE—both the magnetic coercivity and Kerr polarization angle are substantially larger than that of undoped ZnO. It is shown that the magnetic nature of the dopants is responsible for the observed enhanced MO response, which increases with the increasing number of free 3d electron spins, that is, in the order Ni( $\uparrow$ ), Co( $\uparrow\uparrow$ ), and Fe ( $\uparrow\uparrow\uparrow$ ). The dielectric response of the investigated TM-doped ZnO films also depends very strongly on the dopant. The obtained results imply that several polarization mechanisms could be involved to explain the observed behavior. Fe-doped ZnO reveals the strongest dipolar polarization, which may explain the observed ferroelectric-like behavior in this layer.

The obtained results open up a wide perspective for further research. Especially, they give some hints that DMSs may be formed by the used ALD scheme. Moreover, Fe-doped ZnO holds particular promise as it demonstrates the strongest MO response accompanied by a ferroelectric-like behavior; hence, it may possess a true multiferroic nature provided the two properties (ferroelectric and ferromagnetic) are coupled. However, more investigations are needed to get in-depth view and to clarify the phenomena taking place and their dependence on the dopant as well as to outline rational strategy to control them. This also includes the optimization of the ALD scheme to obtain more homogeneous and controllable doping of ZnO.

## ■ ASSOCIATED CONTENT

### SI Supporting Information

The Supporting Information is available free of charge at <https://pubs.acs.org/doi/10.1021/acsomega.2c06240>.

ALD scheme of TM-doped ZnO and O 1s X-ray photoelectron spectroscopy peaks of ZnO and oxygen-deficient ZnO (PDF)

## ■ AUTHOR INFORMATION

### Corresponding Author

Albena Paskaleva — Institute of Solid State Physics, Bulgarian Academy of Sciences, Sofia 1784, Bulgaria; [orcid.org/0000-0002-4409-1915](https://orcid.org/0000-0002-4409-1915); Email: [paskaleva@issp.bas.bg](mailto:paskaleva@issp.bas.bg)

**Authors**

Krastyo Buchkov — Institute of Solid State Physics, Bulgarian Academy of Sciences, Sofia 1784, Bulgaria; Institute of Optical Materials and Technologies, Bulgarian Academy of Sciences, Sofia BG-1113, Bulgaria

Armando Galluzzi — Department of Physics “E.R. Caianiello”, University of Salerno, Fisciano (SALERNO) I-84084, Italy; CNR-SPIN Salerno, Fisciano (SALERNO) I-84084, Italy

Dencho Spassov — Institute of Solid State Physics, Bulgarian Academy of Sciences, Sofia 1784, Bulgaria

Blagoy Blagoev — Institute of Solid State Physics, Bulgarian Academy of Sciences, Sofia 1784, Bulgaria

Tzvetan Ivanov — Institute of Solid State Physics, Bulgarian Academy of Sciences, Sofia 1784, Bulgaria

Vladimir Mehandzhiev — Institute of Solid State Physics, Bulgarian Academy of Sciences, Sofia 1784, Bulgaria

Ivalina Avramova Avramova — Institute of General and Inorganic Chemistry, Bulgarian Academy of Sciences, Sofia BG-1113, Bulgaria

Penka Terzyiska — Institute of Solid State Physics, Bulgarian Academy of Sciences, Sofia 1784, Bulgaria

Peter Tzvetkov — Institute of General and Inorganic Chemistry, Bulgarian Academy of Sciences, Sofia BG-1113, Bulgaria

Daniela Kovacheva — Institute of General and Inorganic Chemistry, Bulgarian Academy of Sciences, Sofia BG-1113, Bulgaria

Massimiliano Polichetti — Department of Physics “E.R. Caianiello”, University of Salerno, Fisciano (SALERNO) I-84084, Italy; CNR-SPIN Salerno, Fisciano (SALERNO) I-84084, Italy

Complete contact information is available at:

<https://pubs.acs.org/10.1021/acsomega.2c06240>

**Notes**

The authors declare no competing financial interest.

**ACKNOWLEDGMENTS**

This work has been financially supported by the Bulgarian National Scientific Fund, Project KP-06-H28/9 and carried out within the framework of the inter-academic Italian-Bulgarian research project—department of Physics “E R Caianiello” CNR-SPIN unit, University of Salerno and the Institute of Solid State Physics “Georgi Nadjakov”, Bulgarian Academy of Sciences.

**REFERENCES**

- (1) Özgür, Ü.; Alivov, Y. I.; Liu, C.; Teke, A.; Reshchikov, M. A.; Doğan, S.; Avrutin, V.; Cho, S. J.; Morkoç, H. A Comprehensive Review of ZnO Materials and Devices. *J. Appl. Phys.* **2005**, *98*, 041301.
- (2) Janotti, A.; Van de Walle, C. G. Fundamentals of Zinc Oxide as a Semiconductor. *Rep. Prog. Phys.* **2009**, *72*, 126501.
- (3) Klingshirn, C. F. ZnO: Material, Physics and Applications. *ChemPhysChem* **2007**, *8*, 782–803.
- (4) Klingshirn, C. ZnO: From Basics towards Applications. *Phys. Status Solidi* **2007**, *244*, 3027–3073.
- (5) Dietl, T.; Ohno, H.; Matsukura, F.; Cibert, J.; Ferrand, D. Zener Model Description of Ferromagnetism in Zinc-Blende Magnetic Semiconductors. *Science* **2000**, *287*, 1019–1022.
- (6) Sato, K.; Katayama-Yoshida, H. Material Design for Transparent Ferromagnets with ZnO-Based Magnetic Semiconductors. *Jpn. J. Appl. Phys.* **2000**, *39*, L555–L558.
- (7) Sluiter, M. H. F.; Kawazoe, Y.; Sharma, P.; Inoue, A.; Raju, A. R.; Rout, C.; Waghmare, U. V. First Principles Based Design and Experimental Evidence for a ZnO-Based Ferromagnet at Room Temperature. *Phys. Rev. Lett.* **2005**, *94*, 187204.
- (8) Ueda, K.; Tabata, H.; Kawai, T. Magnetic and Electric Properties of Transition-Metal-Doped ZnO Films. *Appl. Phys. Lett.* **2001**, *79*, 988.
- (9) Liu, C.; Yun, F.; Morkoç, H. Ferromagnetism of ZnO and GaN: A Review. *J. Mater. Sci. Mater. Electron.* **2005**, *9*, 555–597.
- (10) Pan, F.; Luo, J.; Yang, Y.; Wang, X.; Zeng, F. Giant Piezoresponse and Promising Application of Environmental Friendly Small-Ion-Doped ZnO. *Sci. China Technol. Sci.* **2011**, *S5*, 421–436.
- (11) Pan, F.; Song, C.; Liu, X. J.; Yang, Y. C.; Zeng, F. Ferromagnetism and Possible Application in Spintronics of Transition-Metal-Doped ZnO Films. *Mater. Sci. Eng. R Rep.* **2008**, *62*, 1–35.
- (12) Verma, K. C. Diluted Magnetic Semiconductor ZnO: Magnetic Ordering with Transition Metal and Rare Earth Ions. *Magnetic Materials and Magnetic Levitation*; Sahu, D. R.; Stavrou, V. N., Eds.; Ch. 6, IntechOpen, 2020, DOI: [10.5772/intechopen.90369](https://doi.org/10.5772/intechopen.90369).
- (13) Coey, J. M. D.; Venkatesan, M.; Fitzgerald, C. B. Donor Impurity Band Exchange in Dilute Ferromagnetic Oxides. *Nat. Mater.* **2005**, *4*, 173–179.
- (14) Ando, K.; Saito, H.; Jin, Z.; Fukumura, T.; Kawasaki, M.; Matsumoto, Y.; Koinuma, H. Magneto-Optical Properties of ZnO-Based Diluted Magnetic Semiconductors. *J. Appl. Phys.* **2001**, *89*, 7284.
- (15) Fukuma, Y.; Asada, H.; Yamamoto, J.; Odawara, F.; Koyanagi, T. Large Magnetic Circular Dichroism of Co Clusters in Co-Doped ZnO. *Appl. Phys. Lett.* **2008**, *93*, 142510.
- (16) Varvaro, G.; Di Trolio, A.; Polimeni, A.; Gabbani, A.; Pineider, F.; de Julián Fernández, C.; Barucca, G.; Mengucci, P.; Amore Bonapasta, A.; Testa, A. M. Giant Magneto-Optical Response in H + Irradiated Zn<sub>1-x</sub>Co<sub>x</sub>O Thin Films. *J. Mater. Chem. C* **2019**, *7*, 78–85.
- (17) Zhang, Y. P.; Yan, S. S.; Liu, Y. H.; Ren, M. J.; Fang, Y.; Chen, Y. X.; Liu, G. L.; Mei, L. M.; Liu, J. P.; Qiu, J. H.; Wang, S. Y.; Chen, L. Y. Magneto-Optical Kerr Rotation Enhancement in Co-ZnO Inhomogeneous Magnetic Semiconductor. *Appl. Phys. Lett.* **2006**, *89*, 042501.
- (18) Di Trolio, A.; Polichetti, M.; Polimeni, A.; Testa, A. M. Local Magneto-Optical Response of H+ Irradiated Zn<sub>1-x</sub>CoxO Thin Films. *Eur. Phys. J. Spec. Top.* **2019**, *228*, 683–687.
- (19) Grafke, T.; Grauer, R.; Schäfer, T. The instanton method and its numerical implementation in fluid mechanics. *J. Phys. D Appl. Phys.* **2015**, *48*, 333001.
- (20) Higo, T.; Man, H.; Gopman, D. B.; Wu, L.; Koretsune, T.; van't Erve, O. M. J.; Kabanov, Y. P.; Rees, D.; Li, Y.; Suzuki, M. T.; Patankar, S.; Ikhlas, M.; Chien, C. L.; Arita, R.; Shull, R. D.; Orenstein, J.; Nakatsuji, S. Large Magneto-Optical Kerr Effect and Imaging of Magnetic Octupole Domains in an Antiferromagnetic Metal. *Nat. Photonics* **2018**, *12*, 73–78.
- (21) Kim, D.; Oh, Y.-W.; Kim, J. U.; Lee, S.; Baucour, A.; Shin, J.; Kim, K.-J.; Park, B.-G.; Seo, M.-K. Extreme Anti-Reflection Enhanced Magneto-Optic Kerr Effect Microscopy. *Nat. Commun.* **2020**, *11*, 5937.
- (22) Zhang, S. Y.; Gao, J. L.; Xia, W. B.; Luo, X. J.; Tang, S. L.; Du, Y. W. Giant Magneto-Optical Kerr Effect in HfO<sub>2</sub>/Co/HfO<sub>2</sub>/Al/Silicon Structure. *J. Appl. Phys.* **2013**, *114*, 064308.
- (23) Yamane, H.; Takeda, K.; Kobayashi, M. Magneto-Optical Enhancement and Chemical Sensing Applications of Perpendicular Magnetic CoPt/Ag Stacked Structures with a ZnO Intermediate Layer. *Mater. Trans.* **2016**, *57*, 892–897.
- (24) Yamane, H.; Yasukawa, Y.; Kobayashi, M. Polar Kerr Effect and Perpendicular Magnetic Anisotropy in Fabry-Pérot Cavity Containing CoPt/AZO Magneto-Optical Interference Layer. *J. Appl. Phys.* **2021**, *129*, 203902.
- (25) Konishi, A.; Ogawa, T.; Fisher, C. A. J.; Kuwabara, A.; Shimizu, T.; Yasui, S.; Itoh, M.; Moriwake, H. Mechanism of Polarization

- Switching in Wurtzite-Structured Zinc Oxide Thin Films. *Appl. Phys. Lett.* **2016**, *109*, 102903.
- (26) Joshi, R.; Kumar, P.; Gaur, A.; Asokan, K. Structural, Optical and Ferroelectric Properties of V Doped ZnO. *Appl. Nanosci.* **2014**, *4*, 531–536.
- (27) Yang, Y. C.; Song, C.; Wang, X. H.; Zeng, F.; Pan, F. Cr-Substitution-Induced Ferroelectric and Improved Piezoelectric Properties of  $Zn_{1-x}Cr_xO$  Films. *J. Appl. Phys.* **2008**, *103*, 074107.
- (28) Seol, W. J.; Anoop, G.; Park, H.; Shin, C. W.; Lee, J. Y.; Kim, T. Y.; Kim, W. S.; Joh, H.; Samanta, S.; Jo, J. Y. Ferroelectricity in Solution-Processed V-Doped ZnO Thin Films. *J. Alloys Compd.* **2021**, *853*, 157369.
- (29) Herng, T. S.; Wong, M. F.; Qi, D.; Yi, J.; Kumar, A.; Huang, A.; Kartawidjaja, F. C.; Smadici, S.; Abbamonte, P.; Sánchez-Hanke, C.; Shannigrahi, S.; Xue, J. M.; Wang, J.; Feng, Y. P.; Rusydi, A.; Zeng, K.; Ding, J. Mutual Ferromagnetic–Ferroelectric Coupling in Multiferroic Copper-Doped ZnO. *Adv. Mater.* **2011**, *23*, 1635–1640.
- (30) Sharma, N.; Gaur, A.; Kumar, V.; Kotnala, R. K. Multiferroicity and Magnetoelectric Coupling in Doped ZnO. *Superlattices Microstruct.* **2014**, *65*, 299–308.
- (31) Samanta, A.; Goswami, M. N.; Mahapatra, P. K. Multiferroicity in Mg-Doped ZnO Nanoparticles. *Mater. Sci. Eng., B* **2019**, *245*, 1–8.
- (32) Guziewicz, E.; Godlewski, M.; Krajewski, T.; Wachnicki, Ł.; Szczepaniak, A.; Kopalko, K.; Wójcik-Głodowska, A.; Przeździecka, E.; Paszkowicz, W.; Łusakowska, E.; Kruszewski, P.; Huby, N.; Tallarida, G.; Ferrari, S. ZnO Grown by Atomic Layer Deposition: A Material for Transparent Electronics and Organic Heterojunctions. *J. Appl. Phys.* **2009**, *105*, 122413.
- (33) Pawley, G. S. Unit-Cell Refinement from Powder Diffraction Scans. *J. Appl. Crystallogr.* **1981**, *14*, 357–361.
- (34) Coelho, A. ATOPAS: General Profile and Structure Analysis Software for Powder Diffraction Data. Bruker AXS. (accessed 2022-09-02). <https://www.bruker.com/en/products-and-solutions/diffractometers-and-scattering-systems/x-ray-diffractometers/diffrac-suite-software/difrac-topas.html>.
- (35) Momma, K.; Izumi, F. VESTA 3 for Three-Dimensional Visualization of Crystal, Volumetric and Morphology Data. *J. Appl. Crystallogr.* **2011**, *44*, 1272–1276.
- (36) Qiu, Z. Q.; Bader, S. D. Surface Magneto-Optic Kerr Effect. *Rev. Sci. Instrum.* **2000**, *71*, 1243.
- (37) Paskaleva, A.; Blagoev, B. S.; Terziyska, P. T.; Mehandzhiev, V.; Tzvetkov, P.; Kovacheva, D.; Avramova, I.; Spassov, D.; Ivanova, T.; Gesheva, K. Structural, Morphological and Optical Properties of Atomic Layer Deposited Transition Metal (Co, Ni or Fe)-Doped ZnO Layers. *J. Mater. Sci. Mater. Electron.* **2021**, *32*, 7162–7175.
- (38) Blagoev, B.; Terziyska, P.; Mehandzhiev, V.; Tzvetkov, P.; Kovacheva, D.; Avramova, I.; Ivanova, T.; Gesheva, K.; Paskaleva, A. Optimization of ALD Grown Ni-, Co- and Fe-Doped ZnO Films. *J. Phys. Conf.* **2020**, *1492*, 012053.
- (39) Blagoev, B. S.; Aleksandrova, M.; Terziyska, P.; Tzvetkov, P.; Kovacheva, D.; Kolev, G.; Mehandzhiev, V.; Denishev, K.; Dimitrov, D. Investigation of the Structural, Optical and Piezoelectric Properties of ALD ZnO Films on PEN Substrates. *J. Phys. Conf.* **2018**, *992*, 012027.
- (40) Blagoev, B. S.; Dimitrov, D. Z.; Mehandzhiev, V. B.; Kovacheva, D.; Terziyska, P.; Pavlic, J.; Lovchinov, K.; Mateev, E.; Leclercq, J.; Sveshtarov, P. Electron Transport in Al-Doped ZnO Nanolayers Obtained by Atomic Layer Deposition. *J. Phys. Conf.* **2016**, *700*, 012040.
- (41) Cheary, R. W.; Coelho, A. A Fundamental Parameters Approach to X-Ray Line-Profile Fitting. *J. Appl. Crystallogr.* **1992**, *25*, 109–121.
- (42) Hsu, H. S.; Huang, J. C. A.; Huang, Y. H.; Liao, Y. F.; Lin, M. Z.; Lee, C. H.; Lee, J. F.; Chen, S. F.; Lai, L. Y.; Liu, C. P. Evidence of Oxygen Vacancy Enhanced Room-Temperature Ferromagnetism in Co-Doped ZnO. *Appl. Phys. Lett.* **2006**, *88*, 242507.
- (43) Erskine, J. L.; Stern, E. A. Magneto-Optic Kerr Effect in Ni, Co, and Fe. *Phys. Rev. Lett.* **1973**, *30*, 1329.
- (44) Qureshi, N.; Schmidt, H.; Hawkins, A. R. Cavity Enhancement of the Magneto-Optic Kerr Effect for Optical Studies of Magnetic Nanostructures. *Appl. Phys. Lett.* **2004**, *85*, 431.
- (45) Qiu, Z. Q.; Bader, S. D. Surface Magneto-Optic Kerr Effect. *Rev. Sci. Instrum.* **2000**, *71*, 1243.
- (46) Loughran, T. H.; Keatley, P. S.; Hendry, E.; Barnes, W. L.; Hicken, R. J.; Valkass, R. A.; Yu, W.; Shelford, L. R.; Cavill, S. A.; van der Laan, G.; Dhesi, S. S.; Bashir, M. A.; Gubbins, M. A.; Czoschke, P. J.; Lopusnik, R. Enhancing the Magneto-Optical Kerr Effect through the Use of a Plasmonic Antenna. *Opt. Express* **2018**, *26*, 4738–4750.
- (47) Dong, Y.; Zhang, X. Enhanced Magneto-Optical Kerr Effect in Magnetic Multilayers Containing Double-Negative Metamaterials. *J. Appl. Phys.* **2009**, *105*, 054105.
- (48) Bhowmick, T. K.; De, A.; Lake, R. K. High Figure of Merit Magneto-Optics from Interfacial Skyrmions on Topological Insulators. *Phys. Rev. B: Condens. Matter Mater. Phys.* **2018**, *98*, 024424.
- (49) Kasap, S. *Electrical and Thermal Conduction in Metals*; McGraw Hill, 2001, p 880.
- (50) Lehru, R.; Radhanpura, J.; Kumar, R.; Zala, D.; Vadgama, V. S.; Dadhich, H.; Rathod, V. R.; Trivedi, R. K.; Pandya, D. D.; Shah, N. A.; Solanki, P. S. Studies on Electrical Properties of Fe Doped ZnO Nanostructured Oxides Synthesized by Sol–Gel Method. *Solid State Commun.* **2021**, *336*, 114415.
- (51) Vegesna, S. V.; Bhat, V. J.; Bürger, D.; Dellith, J.; Skorupa, I.; Schmidt, O. G.; Schmidt, H. Increased Static Dielectric Constant in ZnMnO and ZnCoO Thin Films with Bound Magnetic Polarons. *Sci. Rep.* **2020**, *10*, 6698.



CAS BIOFINDER DISCOVERY PLATFORM™

## CAS BIOFINDER HELPS YOU FIND YOUR NEXT BREAKTHROUGH FASTER

Navigate pathways, targets, and diseases with precision

[Explore CAS BioFinder](#)